## SUPPLEMENTARY INFORMATION

# Direct Imaging of Composition-driven Magnetoelastic Phase Transformations in Bulk Fe–Rh

**K. Padrón-Alemán, J. Shen, A. Tengattini, L. Helfen, G.J. Cuello, J.A. Blanco, J.L. Sánchez Llamazares, P. Alvarez-Alonso and Pedro Gorria**

Affiliations

**Institut Laue-Langevin, Grenoble, France**

K. Padrón-Alemán, J. Shen, A. Tengattini, L. Helfen, G.J. Cuello

**Departamento de Física, Universidad de Oviedo, Oviedo, Spain**

K. Padrón-Alemán, J.A. Blanco, P. Alvarez-Alonso, Pedro Gorria

**University Grenoble Alpes, CNRS, Grenoble, France**

A. Tengattini

**Instituto Potosino de Investigación Científica y Tecnológica A.C., San Luis Potosí, México**

J.L. Sánchez Llamazares

**Instituto Universitario de Tecnología Industrial de Asturias, Universidad de Oviedo, Gijón, Spain**

P. Alvarez-Alonso, Pedro Gorria

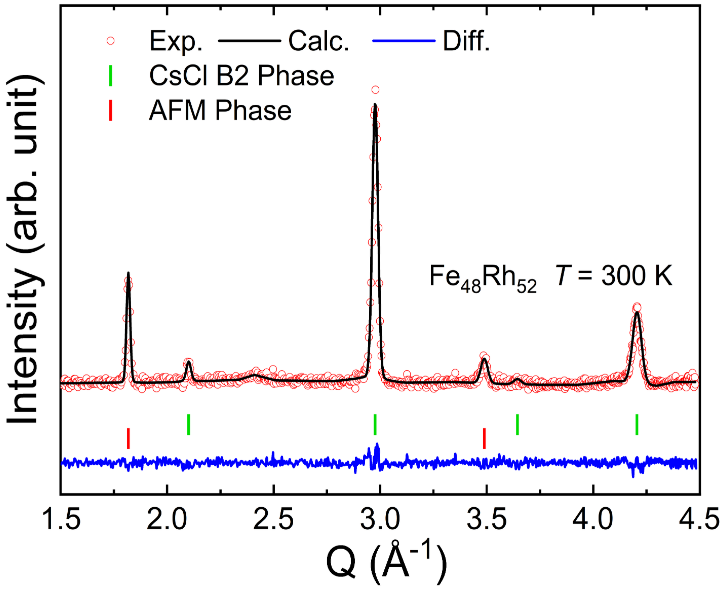

**Fig. S1. Crystal and magnetic structures.** Neutron diffraction pattern of the $Fe_{48}Rh_{52}$ alloy collected at 300 K. Green and red bars indicate the reflections corresponding to the nuclear and magnetic (AFM) structures, respectively.

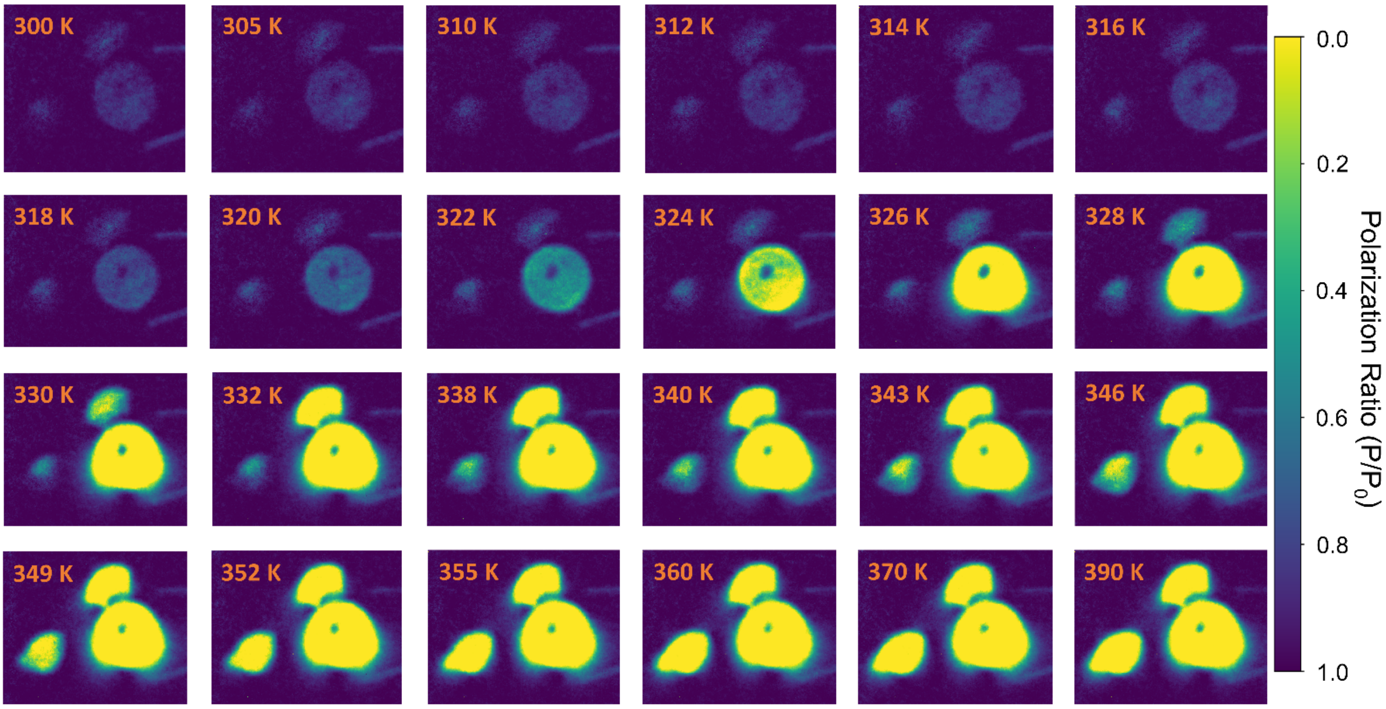

**Fig. S2. AFM-FM depolarization-contrast radiographs.** Depolarization-contrast radiographs resolving the AFM→FM phase transition in equiatomic and near-equiatomic Fe–Rh alloys, obtained using the polarized neutron imaging technique. $Fe_{50}Rh_{50}$ alloy is shown on the left, $Fe_{49}Rh_{51}$ at the top, and $Fe_{48}Rh_{52}$ at the bottom right.

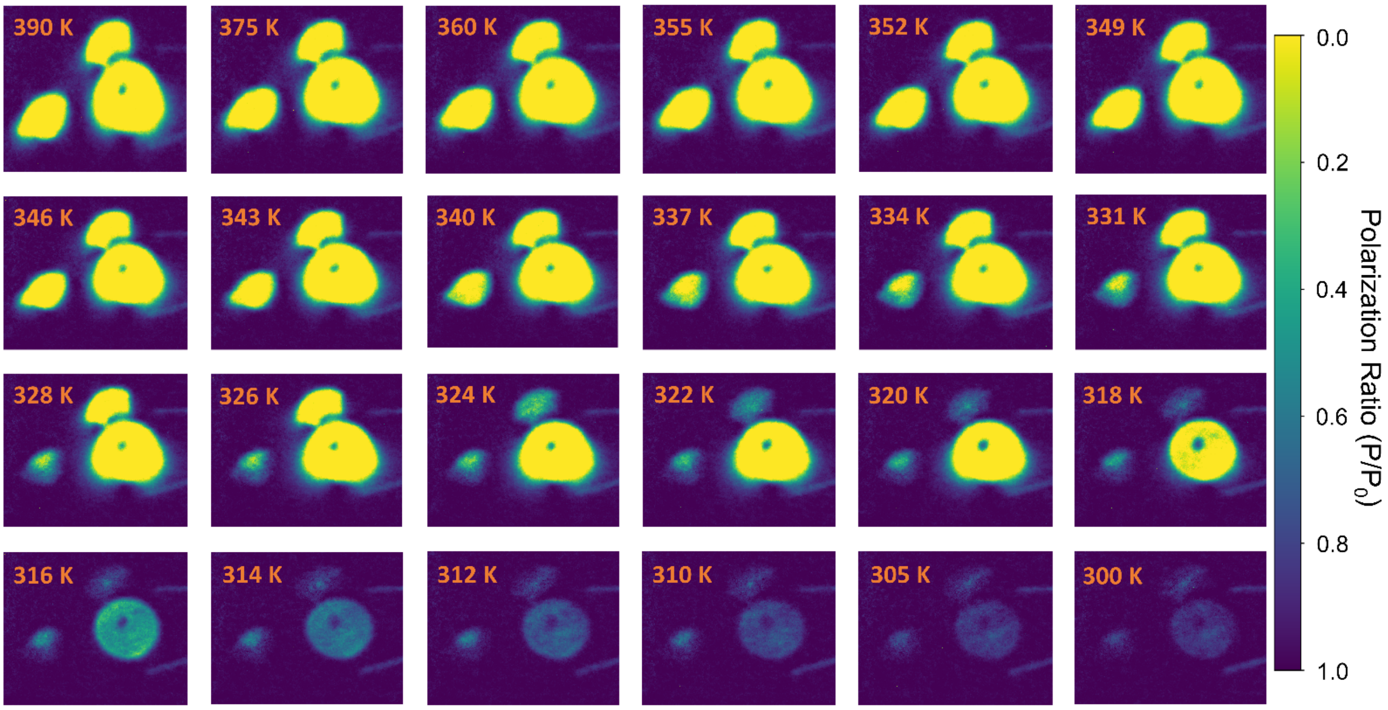

**Fig. S3. FM-AFM depolarization-contrast radiographs.** Depolarization-contrast radiographs resolving the FM→AFM phase transition in equiatomic and near-equiatomic Fe–Rh alloys, obtained using the polarized neutron imaging technique. $Fe_{50}Rh_{50}$ alloy is shown on the left, $Fe_{49}Rh_{51}$ at the top, and $Fe_{48}Rh_{52}$ at the bottom right.

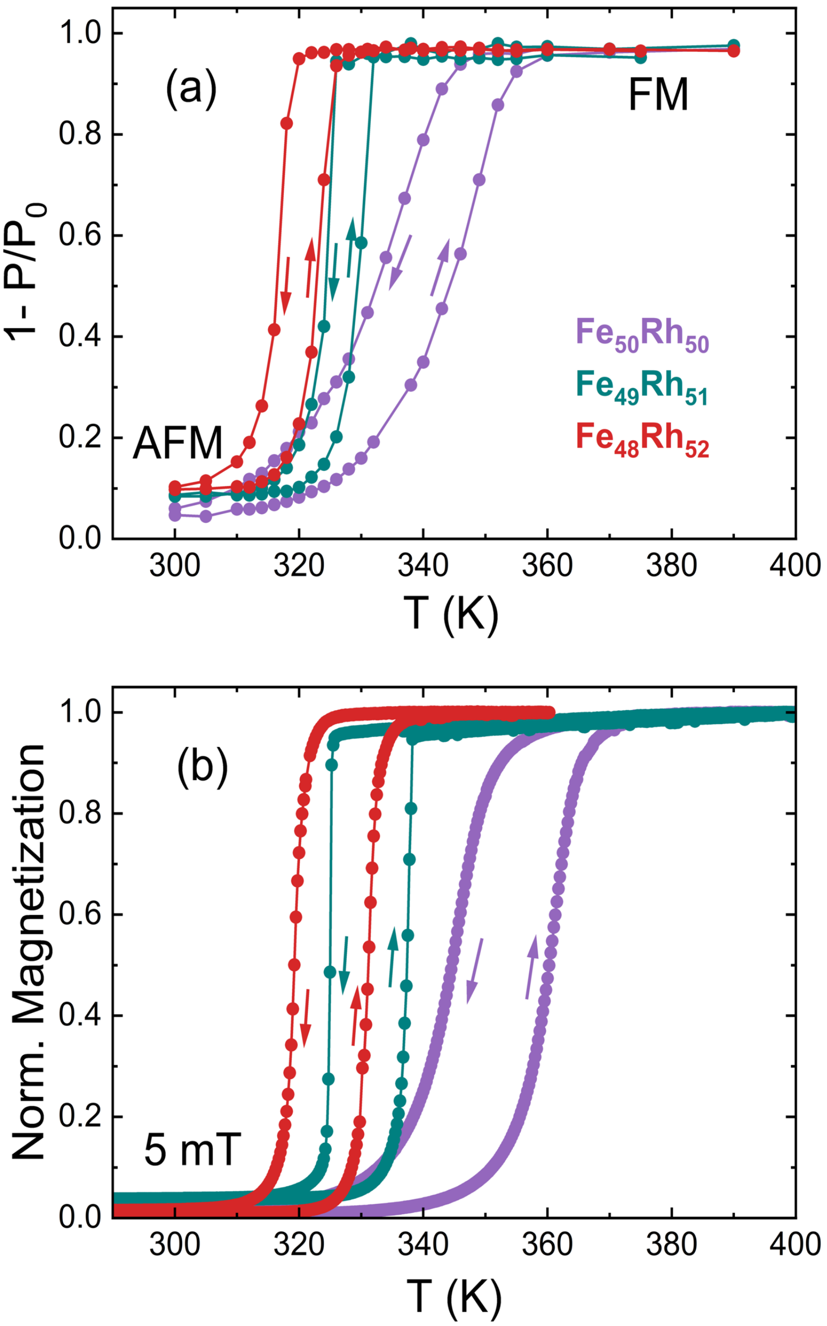

**Fig. S4. Temperature-dependent averaged 1-$P/P_0$ and $M/M^{max}$. a** Temperature dependence of the averaged 1-$P/P_0$ over the full FOV, and **b** normalized 5 mT magnetization curve for $Fe_{50}Rh_{50}$, $Fe_{49}Rh_{51}$, and $Fe_{48}Rh_{52}$ samples. Arrows pointing up and down indicate heating and cooling procedures, respectively.

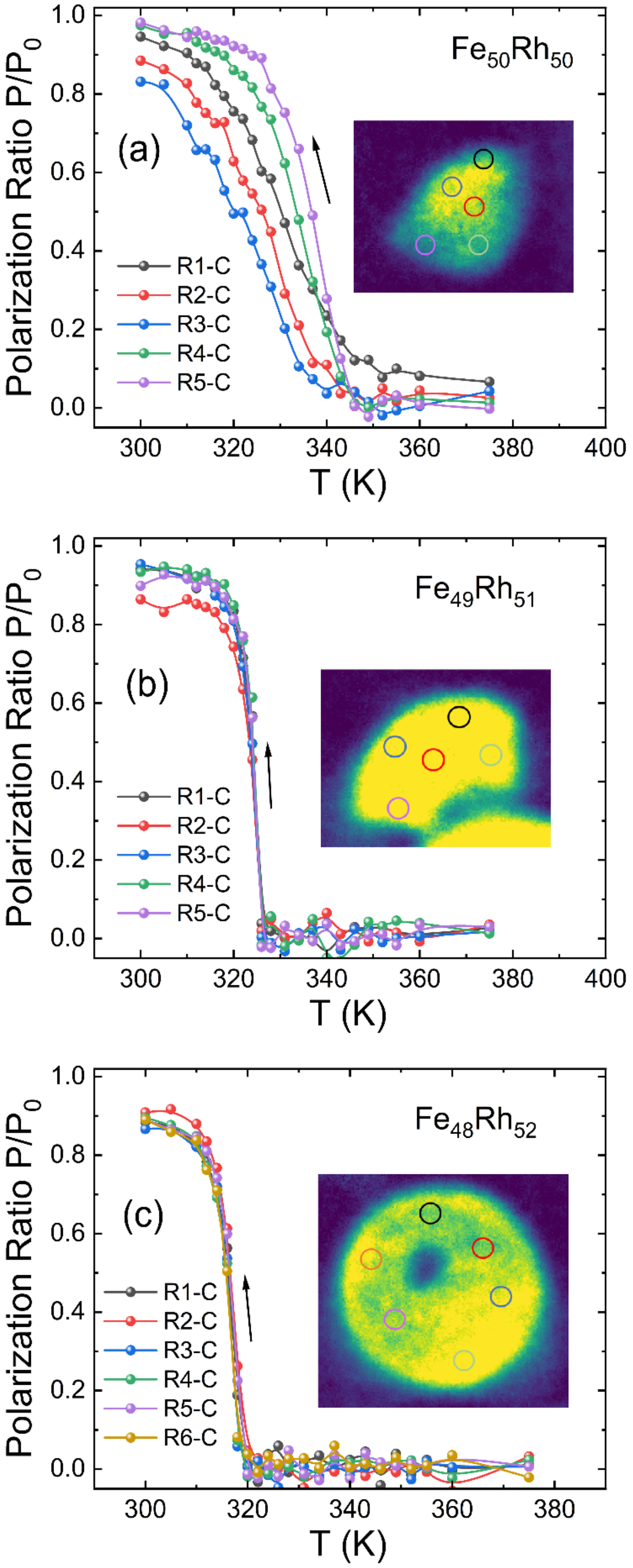

**Fig. S5. Temperature-dependent averaged polarization ratio.** Evolution of the polarization ratio during cooling process calculated from selected areas within the samples for **a** $Fe_{50}Rh_{50}$, **b** $Fe_{49}Rh_{51}$, and **c** $Fe_{48}Rh_{52}$. The black arrows indicate the temperature–change direction. Each encircled area corresponds to a region of 10 pixels in diameter (≈ 570 μm). The accompanying images illustrate the sampled regions (circled).

**Video S1.** The video shows the sequence of depolarization-contrast radiographs presented in Fig. S3 and Fig. S4 during heating (AFM→FM transition) and cooling (FM→AFM transition), respectively.

**Table S1. Relevant Parameters of the Phase Transformation.** Transition temperatures obtained from the low-field $M(T)^{5\ \mathrm{mT}}$ curves. Start ($\mathrm{AF_S}$, $\mathrm{FA_S}$) and finish ($\mathrm{AF_f}$, $\mathrm{FA_f}$) temperatures determined using the tangent method, thermal hysteresis ($\Delta T_{\mathrm{hyst}}$) calculated as $\Delta T_{\mathrm{hyst}} = [\mathrm{AF_S} + \mathrm{AF_f} - (\mathrm{FA_S} + \mathrm{FA_f})]/2$, and $\Delta M$ at the AFM↔FM transition for an applied field of 2 T.

| **Alloy** | **$T_t$ (K) $M(T)^{5\ \mathrm{mT}}$** | **$\mu_0 H$ (T)** | **$\mathrm{AF_S}$ (K)** | **$\mathrm{AF_f}$ (K)** | **$\mathrm{FA_S}$ (K)** | **$\mathrm{FA_f}$ (K)** | **$\Delta T_{\mathrm{hyst}}$ (K)** | **ΔM ($\mathrm{A\ m^2\ kg^{-1}}$)** |
|---|---|---|---|---|---|---|---|---|
| $\mathrm{Fe_{50}Rh_{50}}$ | 352 | 2 | 336 | 369 | 353 | 318 | **17** | **112** |
| $\mathrm{Fe_{49}Rh_{51}}$ | 335 | 2 | 321 | 322 | 309 | 307 | **14** | **123** |
| $\mathrm{Fe_{48}Rh_{52}}$ | 328 | 2 | 313 | 319 | 305 | 300 | **14** | **114** |